



# Design and preparation of easily recycled $\text{Ag}_2\text{WO}_4@\text{ZnO}@\text{Fe}_3\text{O}_4$ ternary nanocomposites and their highly efficient degradation of antibiotics

Juan Shen<sup>1</sup>, Yi Lu<sup>1</sup>, Jin-Ku Liu<sup>1,\*</sup>, and Xiao-Hong Yang<sup>2,\*</sup>

<sup>1</sup>Key Laboratory for Advanced Materials, East China University of Science and Technology, Shanghai 200237, People's Republic of China

<sup>2</sup>Department of Chemistry, Chizhou University, Chizhou 247000, People's Republic of China

Received: 20 April 2016

Accepted: 11 May 2016

Published online:  
19 May 2016

© Springer Science+Business  
Media New York 2016

## ABSTRACT

The  $\text{Ag}_2\text{WO}_4@\text{ZnO}@\text{Fe}_3\text{O}_4$  ternary nanocomposites with high photodegradation activity were synthesized. Compared with  $\text{Ag}_2\text{WO}_4$  and ZnO crystals, the ternary nanocomposites could improve the rate of degrading antibiotics to 152.00 and 143.00 %, respectively. Noticeably, the ternary nanocomposites completely degraded the TH within 1.75 h under sunlight irradiation, which paved a new way for its practical application. The matching of energy-band structure between  $\text{Ag}_2\text{WO}_4$  and ZnO crystals induced an efficient photogenerated electron transfer from the conduction band of ZnO to the conduction band of  $\text{Ag}_2\text{WO}_4$ , leading to valid separation and transfer of photogenerated charge carrier, and the subsequent promotion of photocatalytic activity. Furthermore, the introduction of  $\text{Fe}_3\text{O}_4$  particle not only realized the recycling of catalyst but also enhanced the utilization rate of visible light of  $\text{Ag}_2\text{WO}_4@\text{ZnO}@\text{Fe}_3\text{O}_4$  ternary nanocomposites.

## Introduction

Tetracycline hydrochloride (TH), as a highly effective, bioactive substance, is one of the most primary antibiotic groups used for veterinary adhibition, human therapy as well as agricultural application [1, 2]. However, more than 70.00 % of TH is excreted into the environment in active form after medication, and the TH cannot be self-degraded completely in natural environment [3, 4]. Photocatalytic technology

has been proved to be a highly effective and low-consumptive solution to settle the issue of degrading the TH in recent years [5, 6]. Hence, searching for an efficient photocatalyst is of great significance.

Silver tungstate ( $\text{Ag}_2\text{WO}_4$ ) crystal, as a semiconductor photocatalyst, has been extensively studied due to photocatalytic capability [7, 8] and high quantum efficiency [9, 10], which is expected to be a valid photocatalyst for TH decomposition. However,  $\text{Ag}_2\text{WO}_4$  crystal still has comparatively low degradation efficiency, which could be mainly ascribed to

Address correspondence to E-mails: jkliu@ecust.edu.cn; yxh6110@yeah.net

two drawbacks: (1) the wide band gap of  $\text{Ag}_2\text{WO}_4$  crystal, which leads to the limited light absorption [11]; (2) the lower electron–hole separation, which directly correlates to the lower energy conversion [12, 13]. In recent years, great efforts have been made to quest an approach to overcome these defects, and lots of new technologies have been developed such as heterocoupling [14–19], band engineering [20, 21]. Forming heterostructure is considered to be one of the most efficient ways to enhance the photocatalytic activity.

ZnO crystal has attracted broad interests in scientific and industrial community on account of the merits of its high photoreactivity [22, 23], electrical conductivity [24], and novel photosensitivity [25, 26]. More importantly, the valence band (VB) and conduction band (CB) of  $\text{Ag}_2\text{WO}_4$  crystal are located lower than that of ZnO crystal, which are beneficial for the separation of holes and electrons of  $\text{Ag}_2\text{WO}_4$  and ZnO crystals [27–29]. Therefore, combining  $\text{Ag}_2\text{WO}_4$  with ZnO crystals to form heterostructure is regarded as an effective strategy for enhancing photocatalytic competence, while renewing nanoscale catalyst is difficult [30–35] and magnetic fixation is a good choice to recover catalyst. Therefore,  $\text{Fe}_3\text{O}_4$  material, which has magnetism and strong absorption of visible light, is served as the curing agent of catalysts [36–38].

In this paper, the magnetic  $\text{Ag}_2\text{WO}_4@ZnO@Fe_3O_4$  ternary nanocomposites (simplified as AZF NCs) with high photocatalytic activity were reported. The matching of energy-band structure between  $\text{Ag}_2\text{WO}_4$  and ZnO crystals induced an efficient separation and transfer of photogenerated charge carrier, resulting in the subsequent promotion of photocatalytic activity. Compared with  $\text{Ag}_2\text{WO}_4$  and ZnO crystals, the photocatalytic performance of AZF NCs was increased to 152.00 and 143.00 %, respectively. Furthermore, it took only 1.75 h for the ternary NCs to accomplish the degradation under sunlight, which paved a great path for its practical application. Meanwhile, through compounding the magnetic  $\text{Fe}_3\text{O}_4$  particle with  $\text{Ag}_2\text{WO}_4$  and ZnO crystals, the new ternary NCs could be easily recycled due to its magnetic property. This present work offered a composite photocatalyst for the degradation of antibiotics, and a useful solution for catalyst recycle.

## Experimental sections

### Synthesis of AZF catalyst

#### *Synthesis of $\text{Fe}_3\text{O}_4$ particle*

0.65 g iron chloride hexahydrate and 0.40 g trisodium citrate were dissolved in 40.00 mL of ethylene glycol with stirring for 1 h. Subsequently, 2.40 g sodium acetate was added with stirring for 30 min. The mixture was then sealed in hydrothermal equipment and heated at 200 °C for 12 h. Then, the obtained product was washed with deionized water and ethanol several times, respectively, and then dried under vacuum at 60 °C.

#### *Synthesis of $ZnO@Fe_3O_4$ nanocrystals (NCs)*

Polyethylene glycol-2000 (20.00 mL, 0.05 M) was added to 0.14 g  $\text{Fe}_3\text{O}_4$  particle (dispersed under sonication) with stirring (15 min). Afterward, 1.10 g zinc acetate (dispersed in deionized water) was successively added into the above solution with stirring (30 min). 0.50 g PVP was added to above solution with stirring (15 min) followed by dropwise addition of urea (10.00 mL 1.00 M) with stirring for 1 h. The mixture was transferred into a Teflon-lined autoclave and heated at 180 °C for 12 h. The product was allowed to cool to room temperature naturally, filtered, washed several times with distilled water and ethanol, dried at 120 °C for 6 h, and then calcined at 600 °C for 2 h in a muffle furnace.

#### *Synthesis of AZF NCs*

The deposition of  $\text{Ag}_2\text{WO}_4$  onto ZnO/ $\text{Fe}_3\text{O}_4$  surface was carried out by the precipitation method. 0.05 g ZnO/ $\text{Fe}_3\text{O}_4$  NCs was dispersed in 20.00 mL of deionized water; then 44.00 mL  $\text{Na}_2\text{WO}_4 \cdot 2\text{H}_2\text{O}$  (0.05 M) was added, and the solution was sonicated for 1 h. Subsequently, 44.00 mL  $\text{AgNO}_3$  solution (0.10 M) was dropped into this solution. The resulting product was transferred into a Teflon-lined autoclave and heated at 140 °C for 2 h. The product was allowed to cool to room temperature naturally, filtered, washed several times with distilled water and ethanol, and dried at 50 °C.

## Photodegradation of organic pollutants

The photocatalytic activity of AZF NCs,  $\text{Ag}_2\text{WO}_4$ , and ZnO crystals were evaluated in the degradation of TH. ZnO crystal as a contrast was prepared via combustion method. The photocatalyst (0.10 g) was added into the 30.00 mL of TH solution (10.00 mg/L), completely dispersed in a quartz tube. The system was stirred in the dark to reach the adsorption–desorption equilibrium. And then they were all exposed under Xenon lamp (simulated visible light) and sunlight irradiation, respectively. The reactions were implemented at a room temperature of  $20\text{ }^\circ\text{C} \pm 3\text{ }^\circ\text{C}$  under sunlight irradiation. With the reaction time changing, the UV–Vis absorption spectra of products were tested by a UV-2600 (Shimadzu) spectrometer at room temperature. The degradation rate (%) was calculated by following expression:

$$\text{Degradation (\%)} = C/C_0 \times 100\% \quad (1)$$

where  $C_0$  is the initial concentration of TH after the adsorption–desorption equilibrium and  $C$  is the concentration of TH at  $t$  time. To prevent UV–Vis absorbance of the powder in solution, catalysts were separated from the solution by centrifugation for recycling use.

## Characterizations

The microstructure and morphology were analyzed by transmission electron microscopy (TEM, Hitachi-800). The crystal structure was characterized by X-ray powder diffraction (XRD, Shimadzu XD-3A diffractometer). The actual quantity of element was determined by inductively coupled plasma atomic emission spectroscopy (ICP-AES, Varian, 710 ES). The magnetic measurement was made at room temperature with a Lakeshore 7404 vibrating sample magnetometer (VSM). The ultraviolet visible (UV–Vis) absorption properties of products (solid phase) were tested by UV–Vis spectroscopy (Shimadzu, UV-2600). The structure and thermal property were researched by Fourier transform infrared spectroscopy (Shimadzu, FT-IR Prestige-21). The specific surface area (BET) was determined by isothermal nitrogen adsorption–desorption analysis (Micromeritics ASAP 2400). The photoluminescence (PL) spectrum was investigated using the Varian Eclipse spectrophotometer equipped with Xenon lamp in which the excitation wavelength was 310 nm at room temperature.

## Results and discussions

### Morphologies and structures

The TEM images of AZF NCs and  $\text{ZnO@Fe}_3\text{O}_4$  NCs are shown in Fig. 1. The results showed that they are sphere-like shaped with little aggregation. As can be seen, the diameter of AZF NCs (about 100 nm) was larger than that of  $\text{ZnO@Fe}_3\text{O}_4$  NCs (about 80 nm). And obviously, the morphologies did not change after loading  $\text{Ag}_2\text{WO}_4$  crystal on the surface of  $\text{ZnO@Fe}_3\text{O}_4$  NCs, which indicated the new ternary NCs were successfully prepared.

To investigate the actual element content in AZF NCs, the ICP-AEC was determined. The theoretical and actual contents of Ag, W, Fe, and Zn are shown in Table 1. Remarkably, the actual content of four elements approximated to the theoretical content. The content of Ag, W, Zn, and Fe diminished gradually, which matched the position of  $\text{Ag}_2\text{WO}_4$ , ZnO, and  $\text{Fe}_3\text{O}_4$  crystals in ternary AZF NCs.

FT-IR spectra elucidated the difference in chemical structure among AZF NCs,  $\text{ZnO@Fe}_3\text{O}_4$  NCs,  $\text{Ag}_2\text{WO}_4$ ,  $\text{Fe}_3\text{O}_4$ , and ZnO crystals (Fig. S1, Supporting Information). The FT-IR spectra testified that the structure of  $\text{ZnO@Fe}_3\text{O}_4$  NCs and AZF NCs did not vary during the heterojunction process, which tallied with the analysis of TEM.

All diffraction peaks were in close agreement with the inorganic crystal structure of  $\text{Ag}_2\text{WO}_4$  (JCPDS, No. 34-0061), ZnO (JCPDS, No. 36-1451), and  $\text{Fe}_3\text{O}_4$  (JCPDS, No. 19-0629). The  $\text{Fe}_3\text{O}_4$  crystal revealed broad peaks, owing to the  $\text{Fe}_3\text{O}_4$  particle. The half widths of peaks were relatively large, most likely due to the small size of  $\text{Fe}_3\text{O}_4$  particle [36]. The corresponded diffraction peaks of  $\text{Ag}_2\text{WO}_4$ , ZnO, and  $\text{Fe}_3\text{O}_4$  crystals were explored in both of AZF NCs and  $\text{ZnO@Fe}_3\text{O}_4$  NCs. (The XRD patterns of AZF NCs,  $\text{ZnO@Fe}_3\text{O}_4$  NCs,  $\text{Ag}_2\text{WO}_4$ , ZnO, and  $\text{Fe}_3\text{O}_4$  crystals are shown in Fig. S2, Supporting Information.)

It was noted that along with the formation of AZF NCs, the diffraction peaks of  $\text{Ag}_2\text{WO}_4$ , ZnO, and  $\text{Fe}_3\text{O}_4$  crystals broadened and the crystallinity of intermediate  $\text{ZnO@Fe}_3\text{O}_4$  NCs decreased. It is known that the crystallinity will be debased in the process of generating composite [35], which may lead to the above results. In addition, the amorphous  $\text{Ag}_2\text{WO}_4$  crystal coating on the surface of  $\text{ZnO@Fe}_3\text{O}_4$  NCs led to the crystallinity of AZF NCs further decrease.

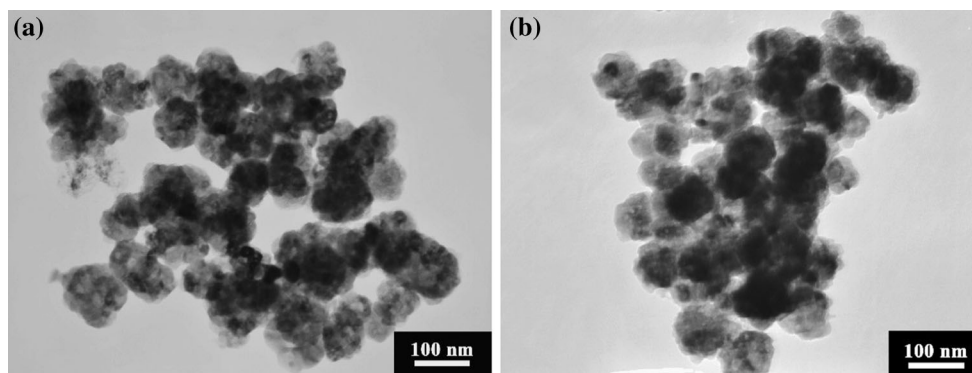


**Figure 1** TEM images of products: **a** AZF NCs and **b** ZnO@Fe<sub>3</sub>O<sub>4</sub> NCs.

**Table 1** The contents of elements in AZF NCs

Sample	Ag	W	Fe	Zn
Theoretical content (/wt%)	44.20	38.00	1.27	2.60
Actual content (/wt%)	46.00	36.00	0.84	2.70

Figure 2 displays the magnetic hysteresis loops of AZF NCs and Ag<sub>2</sub>WO<sub>4</sub> crystal, and all were recorded at 300 K. The hysteresis loop of AZF NCs was normal S-shape, and the “thickness” of the loop reflected the coercivity of AZF NCs. The magnetization saturation ( $M_s$ ) value of AZF NCs was 0.023 emu/mg. The small  $M_s$  could be attributed to the lower content of Fe<sub>3</sub>O<sub>4</sub> crystal, which was only 0.84 % (shown in Table 1) in AZF NCs. The inset shows the coercivity ( $H_c$ ) of AZF NCs which is about 20.00 Oe. The magnetization of Ag<sub>2</sub>WO<sub>4</sub> crystal showed in Fig. 2, confirms the absence of magnetic property of Ag<sub>2</sub>WO<sub>4</sub> crystal. The resulting AZF NCs could be easily

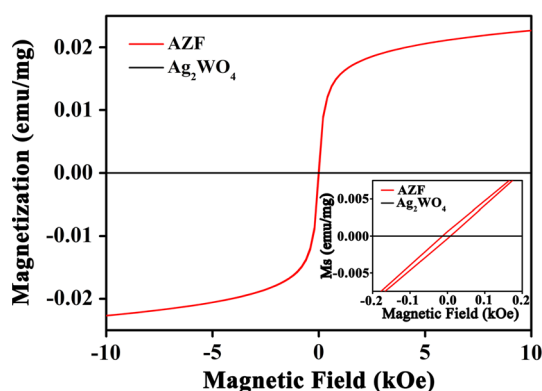


**Figure 2** Magnetic hysteresis loops of AZF NCs and Ag<sub>2</sub>WO<sub>4</sub> crystal. *Inset* expanding region at the field of  $-200$  to  $200$  Oe.

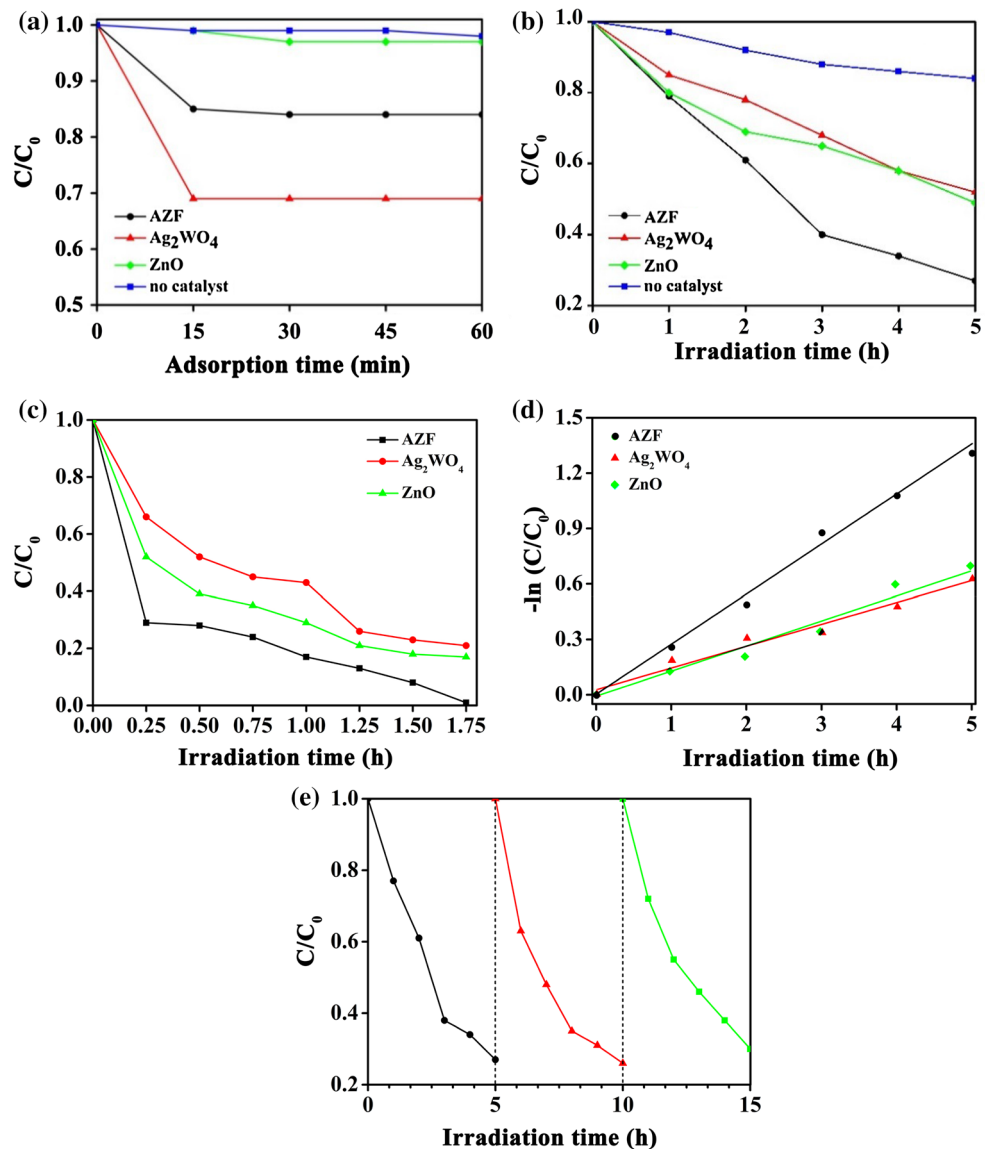
recovered from a dispersed medium due to their magnetic property which suggests a potential application for separation.

### Photocatalytic performance

The photocatalyses of AZF NCs, Ag<sub>2</sub>WO<sub>4</sub>, and ZnO crystals are shown in Fig. 3. As we all know, the adsorption property of photocatalyst toward the degradation contaminants is one of the crucial factors to evaluate the photodegradation activity [3]. The adsorption properties of AZF NCs, Ag<sub>2</sub>WO<sub>4</sub>, and ZnO crystals are measured and presented in Fig. 3a. The adsorption–desorption balance have been achieved between catalyst and antibiotics within 15 min in darkness. Figure 3b shows the photodegradation curves of TH by AZF NCs, Ag<sub>2</sub>WO<sub>4</sub>, and ZnO crystals under Xenon lamp irradiation. The blank test proved that the TH was only slightly degraded in the absence of catalysts, indicating that the self-photolysis of TH can be ignored. The results manifested that compared with pure Ag<sub>2</sub>WO<sub>4</sub> and ZnO crystals, the photocatalytic activity of AZF NCs increased to 152.00 and 143.00 % (calculated by Eq. 1), respectively.

In order to verify the practical application of the new NCs catalyst, the photodegradation of TH was investigated under sunlight irradiation. As shown in Fig. 3c, the AZF NCs also exhibited the strongest photodegradation capability, which could complete the degradation within just 1.75 h, while Ag<sub>2</sub>WO<sub>4</sub> and ZnO crystals degraded less. From the above, Fig. 3b, c demonstrates that combining Ag<sub>2</sub>WO<sub>4</sub> with ZnO and Fe<sub>3</sub>O<sub>4</sub> crystals to form ternary nanostructure could remarkably enhance the degradation efficiency. And the degradation rate of TH by AZF NCs

**Figure 3** **a** Adsorption properties of the as-synthesized products under dark condition. **b, c** The photodegradation curves of TH solution by using AZF, Ag<sub>2</sub>WO<sub>4</sub>, and ZnO catalysts under Xenon lamp and sunlight irradiation, respectively. **d** The first-order kinetic plots of the obtained products for TH degradation. **e** Reusability of the ternary NCs for three successive runs.



under sunlight was much faster than Xenon lamp irradiation. The results further demonstrated that AZF NCs had the capability to meet the demand of practical applications.

Fig. 3d shows that the reaction belonged to pseudo first-order kinetics, called Langmuir–Hinshelwood (L–H) [2]. The relevant equations are listed as follows:

$$r = -dC/dt = k_r K_a C / (1 + K_a C) \tag{2}$$

where  $r$  is the reaction rate,  $k_r$  is the reaction rate constant,  $K_a$  is the adsorption coefficient, and  $C$  is the

reactant concentration. If the concentration of pollutants is low, Eq. 3 can be obtained.

$$\ln(C_0/C) = kt \tag{3}$$

$C_0$  is the initial dye concentration,  $C$  is the dye concentration at  $t$  irradiation time, and  $k$  is the apparent first-order rate constant. Obviously, AZF NCs had the best photodegradation performance. The rate constants ( $k$ ) of AZF NCs, Ag<sub>2</sub>WO<sub>4</sub>, and ZnO crystals were calculated, which were 0.27, 0.12, and 0.14 min<sup>-1</sup>, respectively. The results showed great agreement with the data discussed above.

Furthermore, the stability of a photocatalyst determines its service lifetime and practical application value. Figure 3e shows the stability of AZF NCs by photodegrading TH for three cycles. No significant variation in photodegradation activity can be observed after 15 h irradiation. Results shown in Fig. 3 demonstrate that the introduction of ZnO crystal can remarkably increase both the photodegradation performance and the stability of  $\text{Ag}_2\text{WO}_4$  crystal.

## Photodegradation mechanism

### Band-gap features and BET

To explore the photocatalytic mechanism, the energy-band and band-edge features were investigated via UV–Vis absorption spectra, photoluminescence spectra, and  $\text{N}_2$  adsorption–desorption isotherm.

Figure 4a shows that AZF NCs exhibit an absorption enhancement in band edge of 400–700 nm compared with  $\text{Ag}_2\text{WO}_4$  and ZnO crystals, which was ascribed to their matching energy-band. Meanwhile, the composite of  $\text{Fe}_3\text{O}_4$  crystal could also improve the performance of utilizing visible light, which enhances the excited energy for photodegradation. It should be pointed out that the superior optical property of AZF NCs with wide absorption band made it suitable in both sunny and cloudy conditions.

For a semiconductor, the optical absorption near the band edge follows:

$$\alpha h\nu = A(h\nu - E_g)^{n/2} \quad (4)$$

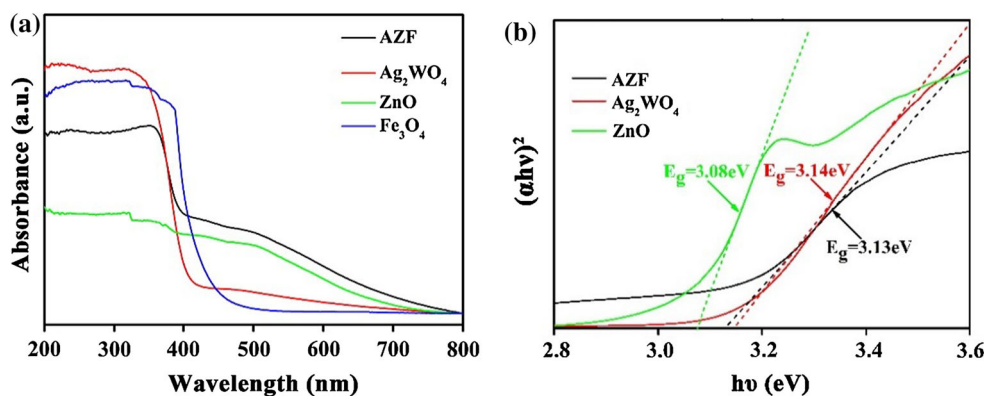
where  $\alpha$ ,  $\nu$ ,  $A$ ,  $E_g$ , and  $n$  are absorption coefficient, light frequency, proportionality constant, band gap, and an integer, respectively. After calculation, the  $E_g$  values of AZF NCs,  $\text{Ag}_2\text{WO}_4$ , and ZnO crystals were

3.13, 3.14, and 3.08 eV, respectively, as shown in Fig. 4b. It testifies that the interfacial structure between  $\text{Ag}_2\text{WO}_4$  and ZnO crystals diminished the energy-band, which can enhance visible light absorption of AZF NCs, and facilitate the photodegradation.

Photoluminescence (PL) spectrum is a well-known technique to investigate both transfer of the interface charge carrier and recombination of the electron–hole pairs [39]. The weaker intensity represents lower recombinative rate of charge carrier, leading to a higher photocatalytic activity [40]. The excellent electrical conductivity of ZnO crystal could facilitate the delivering of the photo-induced charge carriers to the active sites, resulting in a reduction in charge combination for the composite photocatalyst containing ZnO crystal [41]. The ZnO crystal paved a path for efficient transfer of photo-excited electrons from ZnO to  $\text{Ag}_2\text{WO}_4$  crystals and effectively consumed photo-induced interfacial charge transfer, thus suppressing the recombination of photo-induced electron–hole pairs [42]. Compared with PL emission peaks of  $\text{Ag}_2\text{WO}_4$  crystal and AZF NCs, the PL intensity of AZF NCs at the range of 400–466 nm receded apparently, revealing that the charge combination was further reduced in ternary NCs. This quenching effect attributes to well distribution, small size, and large surface area in the ternary composite, by the synergistic effect between ZnO and  $\text{Ag}_2\text{WO}_4$  crystals.

Figure 5b shows  $\text{N}_2$  adsorption–desorption isotherm of AZF NCs. The surface area of  $\text{Ag}_2\text{WO}_4$  crystal was  $1.08 \text{ m}^2/\text{g}$  [8]. The surface area of AZF NCs was  $13.0 \text{ m}^2/\text{g}$ . Hence, the introduction of ZnO crystal increased the surface area of  $\text{Ag}_2\text{WO}_4$  crystal, which can provide more active sites for reaction with

**Figure 4** UV–Vis spectra of AZF NCs,  $\text{Ag}_2\text{WO}_4$ , ZnO, and  $\text{Fe}_3\text{O}_4$  crystals.



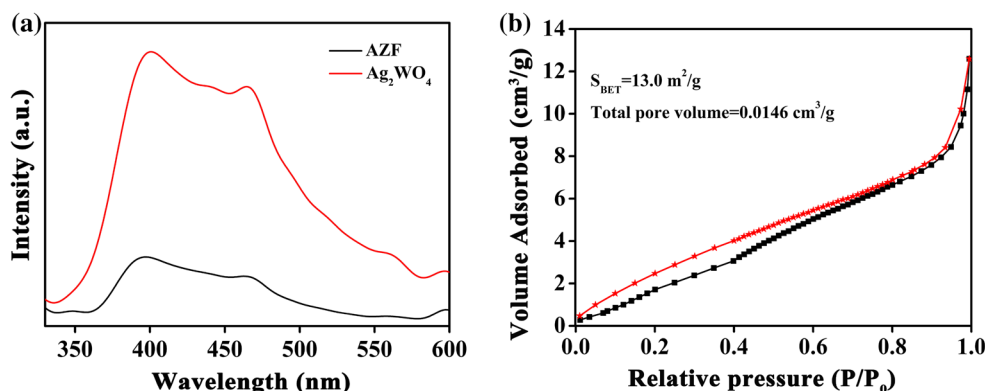


**Figure 5** a Photoluminescence spectra of AZF NCs and Ag<sub>2</sub>WO<sub>4</sub> crystal. b N<sub>2</sub> adsorption–desorption isotherm of AZF NCs.

TH molecules, thus favoring the enhancement in photodegradation.

*Photocatalytic mechanism*

The enhanced catalytic activity of AZF catalyst attributes to the synergistic-compound effect of Ag<sub>2</sub>WO<sub>4</sub> and ZnO crystals due to their matching energy-band structure. To demonstrate efficient separation of the charge carrier, the VB and CB potentials of Ag<sub>2</sub>WO<sub>4</sub> and ZnO crystals were calculated according to Eqs. 5 and 6.

$$E_{VB} = X - E_c + 0.50 E_g \tag{5}$$

$$E_{CB} = E_{VB} - E_g \tag{6}$$

where X is the geometric mean of Mulliken electronegativity of the constituent atoms in the semiconductor, E<sub>c</sub> is the energy of free electrons on the hydrogen scale (4.50 eV) [43], E<sub>VB</sub> and E<sub>CB</sub> are the edge potential value of VB and CB, respectively. E<sub>g</sub> represents the band gap of sample. On the basis of the Mott–Schottky equation (Eq. 4), the E<sub>g</sub> values of Ag<sub>2</sub>WO<sub>4</sub>, ZnO crystals were 3.14 and 3.08 eV, respectively (shown in Fig. 4b). X (Ag<sub>2</sub>WO<sub>4</sub>) = 6.00 eV, X (ZnO) = 5.79 eV. After calculation, E<sub>VB</sub> (Ag<sub>2</sub>WO<sub>4</sub>) = 3.07 eV, E<sub>CB</sub> (Ag<sub>2</sub>WO<sub>4</sub>) = -0.11 eV, E<sub>VB</sub> (ZnO) = 2.90 eV, E<sub>CB</sub> (ZnO) = -0.18 eV. Therefore, the formation of the ternary NCs not only narrows the band gap but also effects the position of band edge. The results indicated that the interfacial charge-transfer interaction between Ag<sub>2</sub>WO<sub>4</sub> and ZnO crystals was of great benefit to the degradation activity and stability of photocatalyst. The above-mentioned results well

matched with the photodegradation analysis (as shown in Fig. 3).

Herein, the mechanism of the enhancing photocatalytic activity and stability of AZF NCs is proposed (Fig. 6). When Ag<sub>2</sub>WO<sub>4</sub> and ZnO crystals were irradiated by light, the electrons can be excited from VB to CB, leaving the holes on the VB. Due to the interfacial electron transfer effect and the matching energy-band, these photogenerated electrons on the CB of ZnO crystal tend to transfer to Ag<sub>2</sub>WO<sub>4</sub> crystal, resulting in efficient electron–hole pair separation, enhancing photocatalytic activity [44]. The electrons on the CB of Ag<sub>2</sub>WO<sub>4</sub> crystal further reacted with oxygen molecules to form superoxide ions (O<sup>•−</sup>). Meanwhile, the leaving photogenerated holes in Ag<sub>2</sub>WO<sub>4</sub> crystal transferred to the VB of ZnO crystal, and further reacted with absorbed H<sub>2</sub>O molecules to produce

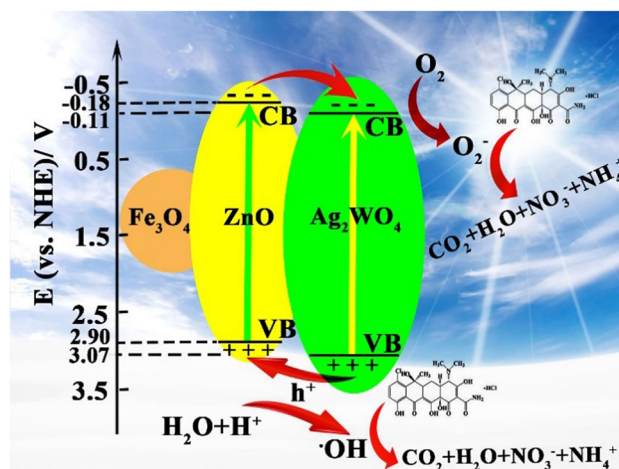


**Figure 6** The photocatalytic mechanism of AZF catalyst.

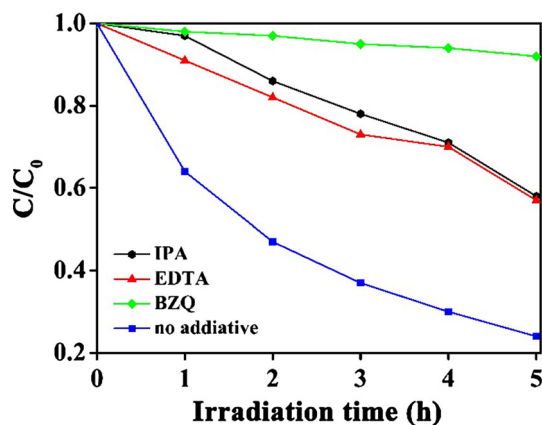


**Figure 7** TH degradation curves with different added trapping agents.

active oxidants such as hydroxyl radicals ( $\cdot\text{OH}$ ). The generated  $\text{O}_2^-$ ,  $\cdot\text{OH}$ , and holes had intense oxidation ability to oxidize antibiotic in photodegradation process, leading to dramatic photocatalytic performance [45]. Hence, the synergistic effect of the matching energy-band and the interfacial electron transfer effect between  $\text{ZnO}$  and  $\text{Ag}_2\text{WO}_4$  crystals can effectively promote photo-induced charge carriers separation and enhance the photocatalytic activity of catalyst. The major routes photodegrading the TH are proposed as shown in Scheme S1 (Supporting Information).

To further reveal the roles of the active species on the photocatalytic process, isopropanol (IPA), *p*-benzoquinone (BZQ), and ethylene diamine tetraacetic acid (EDTA) were employed as scavengers for hydroxyl radicals ( $\cdot\text{OH}$ ), superoxide anion radicals ( $\text{O}_2^-$ ), and photogenerated holes ( $h^+$ ), respectively. Figure 7 shows that the addition of BZQ into the photocatalytic system caused fast deactivation of AZF NCs, indicating  $\text{O}_2^-$  is the predominant active species. Moreover, the introduction of IPA and EDTA into the photocatalytic system could also decrease the photocatalytic degradation of TH, suggesting  $\cdot\text{OH}$  and  $h^+$  also played an important role in the photocatalytic process. The result coincided with the photocatalytic mechanism shown in Fig. 6.

### Application of AZF NCs

Figure 8 presents the process of degrading antibiotic wastewater and recovering AZF catalyst. The whole process constitutes three steps: Step 1, the simulate effluent of TH solution was degraded by AZF NCs under sunlight; Step 2, after photodegradation process, the AZF catalyst was recovered through

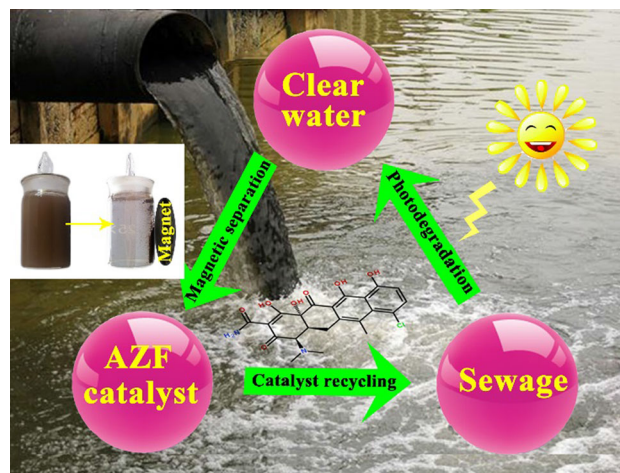


**Figure 8** Water purification system under sunlight by AZF NCs.

magnetic separation (shown in Inset); Step 3, the catalyst could be reused after it was filtered, washed several times with distilled water and ethanol. The application of the reported water purification system would realize the catalyst recycling, as well as reduce the cost. More importantly, it could be flexibly used to degrade different antibiotics by the effective catalyst.

### Conclusions

In summary, AZF NCs with wide absorption band and highly efficient photocatalytic activity were prepared and they could be easily recycled due to their magnetic property. The matching of energy-band structure between  $\text{Ag}_2\text{WO}_4$  and  $\text{ZnO}$  crystals enhanced an efficient separation and transfer of photogenerated charge carrier, leading to the succeeding elevation of photocatalytic activity. Compared with  $\text{Ag}_2\text{WO}_4$  crystal, AZF NCs improved the degradation rate to 152.00 %. In addition, the ternary-nanocomposite could completely degrade the TH within 1.75 h under sunlight irradiation, which certified that the new ternary NCs gratified the demand of practical application, which was desirable to the value in engineering application. The general thought of designing the ternary NCs is of great referential significance for preparing other functional materials.

### Acknowledgements

This work was supported by the National Natural Science Foundation of China (Grant 21341007),



Fundamental Research Funds for the Central Universities (Grant 222201313005), and State Key Laboratory of Pollution Control and Resource Reuse Foundation (Grant 13019).

**Electronic supplementary material:** The online version of this article (doi:[10.1007/s10853-016-0063-9](https://doi.org/10.1007/s10853-016-0063-9)) contains supplementary material, which is available to authorized users.

## References

- [1] Ocampo-Pérez R, Rivera-Utrilla J, Gómez-Pacheco C, Sánchez-Polo M, López-Peñalver JJ (2012) Kinetic study of tetracycline adsorption on sludge-derived adsorbents in aqueous phase. *Chem Eng J* 213:88–96
- [2] Li XY, Wang LP, Xu DB, Lin DB, Li P, Lin S, Shi WD (2015) Enhanced photocatalytic degrassation activity for tetracycline under visible light irradiation of Ag/Bi<sub>3.84</sub>W<sub>0.16</sub>O<sub>6.24</sub> nanooctahedrons. *CrystEngComm* 17:2421–2428
- [3] Xu DF, Cheng B, Cao SW, Yu JG (2015) Enhanced photocatalytic activity and stability of Z-scheme Ag<sub>2</sub>CrO<sub>4</sub>–GO composite photocatalysts for organic pollutant degradation. *Appl Catal B Environ* 164:380–388
- [4] Jo WN, Clament Sagaya Selvam N (2015) Enhanced visible light-driven photocatalytic performance of ZnO–g–C<sub>3</sub>N<sub>4</sub> coupled with graphene oxide as a novel ternary nanocomposite. *J Hazard Mater* 299:462–470
- [5] Bai YY, Lu Y, Liu JK (2016) An efficient photocatalyst for degradation of various organic dyes: Ag@Ag<sub>2</sub>MoO<sub>4</sub>–AgBr composite. *J Hazard Mater* 307:26–35
- [6] Zhou MJ, Han DL, Liu XL, Ma CC, Wang HQ, Tang YF, Huo PW, Shi WD, Yan YS, Yang JH (2015) Enhanced visible light photocatalytic activity of alkaline earth metal ions-doped CdSe/GO photocatalysts synthesized by hydrothermal method. *Appl Catal B Environ* 172:174–184
- [7] Roca RA, Sczancoski JC, Nogueira IC, Fabbro MT, Alves HC, Gracia L, Santos LPS, Sousa CP, Andrés J, Luz GE Jr, Longo E, Cavalcante LS (2015) Facet-dependent photocatalytic and antibacterial properties in  $\alpha$ -Ag<sub>2</sub>WO<sub>4</sub> crystals: combining experimental data and theoretical insights. *Catal Sci Technol* 5(8):4091–4107
- [8] Chen HH, Xu YM (2014) Photoactivity and stability of Ag<sub>2</sub>WO<sub>4</sub> for organic degradation in aqueous suspensions. *Appl Surf Sci* 319:319–323
- [9] Lin ZY, Li JL, Zheng ZQ, Yan JH, Liu P, Wang CX, Yang GW (2015) Electronic reconstruction of  $\alpha$ -Ag<sub>2</sub>WO<sub>4</sub> nanorods for the visible-light photocatalysis. *ACS Nano* 9:7256–7265
- [10] Wang QP, Guo XX, Wu WH, Liu SX (2011) Preparation of fine Ag<sub>2</sub>WO<sub>4</sub> antibacterial powders and its application in the sanitary ceramics. *Adv Mater Res* 284–286:1321–1325
- [11] Vignesh K, Kang M (2015) Facile synthesis, characterization and recyclable photocatalytic activity of Ag<sub>2</sub>WO<sub>4</sub>@g–C<sub>3</sub>N<sub>4</sub>. *Mater Sci Eng B* 199(5):30–36
- [12] Pinatti IM, Nogueira IC, Pereira WDS, Pereira PFS, Gonçalves RF, Varela JA, Longo E, Rosa ILV (2015) Structural and photoluminescence properties of Eu<sup>3+</sup> doped  $\alpha$ -Ag<sub>2</sub>WO<sub>4</sub> synthesized by the green coprecipitation methodology. *Dalton Trans* 44:17673
- [13] Zhang XY, Wang JD, Liu JK, Yang XH, Lu Y (2014) Constructing of silver tungstate multilevel sphere clusters by controlling energy distribution on crystal surface. *CrystEngComm* 17:1129–1138
- [14] Pereira WD, Andrés J, Gracia L, San-Miguel MA, da Silva EZ, Longo E, Longo VM (2015) Elucidating the real-time Ag nanoparticle growth on  $\alpha$ -Ag<sub>2</sub>WO<sub>4</sub> during electron beam irradiation: experimental evidence and theoretical insights. *Phys Chem Chem Phys* 17:5352–5359
- [15] Longo VM, Foggi CCD, Ferrer MM, Gouveia AF, Andre RS, Avansi W, Vergani CE, Machado AL, Andrés J, Cavalcante LS, Hernandes AC, Longo E (2014) Potentiated electron transference in  $\alpha$ -Ag<sub>2</sub>WO<sub>4</sub> microcrystals with Ag nanofilaments as microbial agent. *J Phys Chem A* 118:5769–5778
- [16] Longo E, Volanti DP, Longo VM, Gracia L, Nogueira IC, Almeida MAP, Pinheiro AN, Ferrer MM, Cavalcante LS, Andrés J (2014) Toward an understanding of the growth of Ag filaments on  $\alpha$ -Ag<sub>2</sub>WO<sub>4</sub> and their photoluminescent properties: a combined experimental and theoretical study. *J Phys Chem C* 118:1229–1239
- [17] Zhu Z, Yan Y, Li J (2016) One-step synthesis of flower-like WO<sub>3</sub>/Bi<sub>2</sub>WO<sub>6</sub> heterojunction with enhanced visible light photocatalytic activity. *J Mater Sci* 51(4):2112–2120
- [18] Li JJ, Yu CY, Zheng CC, Etogo A, Xie YL, Zhong YJ, Hu Y (2015) Facile formation of Ag<sub>2</sub>WO<sub>4</sub>/AgX (X = Cl, Br, I) hybrid nanorods with enhanced visible-light-driven photoelectrochemical properties. *Mater Res Bull* 61:315–320
- [19] Liu XH, Hu JL, Li JJ, Hu Y, Shao Y, Yang HJ, Tong GX, Qian HS (2013) Facile synthesis of Ag<sub>2</sub>WO<sub>4</sub>/AgCl nanorods for excellent photocatalytic properties. *Mater Lett* 91:129–132
- [20] Yang KS, Dai Y, Huang BB, Whangbo MH (2008) Density functional characterization of the band edges, the band gap states, and the preferred doping sites of halogen-doped TiO<sub>2</sub>. *Chem Mater* 20:6528–6534

- [21] Wang DF, Kako T, Ye JH (2009) New series of solid-solution semiconductors  $(\text{AgNbO}_3)_{1-x}(\text{SrTiO}_3)_x$  with modulated band structure and enhanced visible-light photocatalytic activity. *J Phys Chem C* 113:3785–3792
- [22] Djuricic AB, Chen XY, Leung YH, Ng AMC (2012) ZnO nanostructures: growth, properties and applications. *J Mater Chem* 22:6526–6535
- [23] Khadem-Hosseini A, Mirabedini SM, Pazokifard S (2015) Photocatalytic activity and colloidal stability of various combinations of  $\text{TiO}_2/\text{SiO}_2$  nanocomposites. *J Mater Sci* 51(6):8317–8325
- [24] Zhang Q, Liu JK, Wang JD, Luo HX, Yi L, Yang XH (2014) Atmospheric self-induction synthesis and enhanced visible light photocatalytic performance of  $\text{Fe}^{3+}$  doped Ag-ZnO mesocrystals. *Ind Eng Chem Res* 53:13236–13246
- [25] Deng YJ, Lu Y, Liu JK, Yang XH (2015) Mass production and photoelectric performances of P and Al Co-doped ZnO nanocrystals under different cooling post-processes. *J Alloy Compd* 648:438–444
- [26] Wang JD, Liu JK, Tong Q, Lu Y, Yang XH (2014) High degradation activity and quantity production of aluminum-doped zinc oxide nanocrystals modified by nitrogen atoms. *Ind Eng Chem Res* 53:2229–2237
- [27] Deng YJ, Lu Y, Liu JK, Yang XH (2015) Production and photoelectric activity of P and Al co-doped ZnO nanomaterials. *Eur J Inorg Chem* 22:3708–3714
- [28] Zhang XY, Liu JK, Wang JD, Yang XH (2015) Mass production, enhanced visible light photocatalytic efficiency, and application of modified ZnO nanocrystals by carbon dots. *Ind Eng Chem Res* 54(6):1766–1772
- [29] Zhang Q, Wan Q, Dai G, Zhou C, Zou B (2011) Controllable ZnO architectures by ethanolamine-assisted hydrothermal reaction for enhanced photocatalytic activity. *J Phys Chem C* 115:2769–2775
- [30] Miguel-Sancho N, Bomati-Miguel O, Roca AG, Martinez G, Arruebo M, Santamaria J (2012) Synthesis of magnetic nanocrystals by thermal decomposition in glycol media: effect of process variables and mechanistic study. *Ind Eng Chem Res* 51(25):8348–8357
- [31] Miguel-Sancho N, Bomati-Miguel O, Colom Glòria et al (2011) Development of stable, water-dispersible, and bio-functionalizable superparamagnetic iron oxide Nanoparticles. *Chem Mater* 23(11):2795–2802
- [32] Bian SW, Si L, Lan C (2015) Synthesis of magnetically recyclable  $\text{Fe}_3\text{O}_4$  @polydopamine-Pt composites and their application in hydrogenation reactions. *J Mater Sci* 51(7):1–7
- [33] Karunakaran C, Vinayagamoorthy P, Jayabharathi J (2014) Nonquenching of charge carriers by  $\text{Fe}_3\text{O}_4$  core in  $\text{Fe}_3\text{O}_4/\text{ZnO}$  nanosheet photocatalyst. *Langmuir* 30(49):15031–15039
- [34] Liu YS, Wei SH, Wei G (2015) Ag/ZnO heterostructures and their photocatalytic activity under visible light: effect of reducing medium. *J Hazard Mater* 287:59–68
- [35] Shylesh S, Schunemann V, Thiel WR (2010) Magnetically separable nanocatalysts: bridges between homogeneous and heterogeneous catalysis. *Angew Chem Int Ed* 49:3428–3459
- [36] Feng X, Guo H, Patel K, Zhou H, Lou X (2014) High performance, recoverable  $\text{Fe}_3\text{O}_4$ -ZnO nanoparticles for enhanced photocatalytic degradation of phenol. *Chem Eng J* 244:327–334
- [37] Liu H, Wu J, Min JH, Zhang X, Kim YK (2013) Tunable synthesis and multifunctionalities of  $\text{Fe}_3\text{O}_4$ -ZnO hybrid core-shell nanocrystals. *Mater Res Bull* 48:551–558
- [38] Zhu Z, Lu Z, Wang DD, Tang X, Yan YS, Shi WD, Wang YS, Gao NL, Yao X, Dong HJ (2016) Construction of high-dispersed Ag/ $\text{Fe}_3\text{O}_4$ /g- $\text{C}_3\text{N}_4$  photocatalyst by selective photo-deposition and improved photocatalytic activity. *Appl Catal B Environ* 182:115–122
- [39] Mueses MA, Machuca-Martinez F, Puma GL (2013) Effective quantum yield and reaction rate model for evaluation of photocatalytic degradation of water contaminants in heterogeneous pilot-scale solar photoreactors. *Chem Eng J* 215(2):937–947
- [40] Liu Q, Guo YR, Chen ZH, Zhang ZG, Fang XM (2016) Constructing a novel ternary Fe(III)/graphene/g- $\text{C}_3\text{N}_4$  composite photocatalyst with enhanced visible-light driven photocatalytic activity via interfacial charge transfer effect activity via interfacial charge transfer effect. *Appl Catal B Environ* 183:231–241
- [41] Di J, Xia JX, Ge YP, Li HP, Ji HY, Xu H, Zhang Q, Li HM, Li ML (2015) Novel visible-light-driven CQDs/ $\text{Bi}_2\text{WO}_6$  hybrid materials with enhanced photocatalytic activity toward organic pollutants degradation and mechanism insight. *Appl Catal B Environ* 168:51–61
- [42] Wang FR, Su YY, Liu JK et al (2016) Enhanced photoelectric properties by the coordinating role of doping and modification. *Phys Chem Chem Phys* 18:4850–4859
- [43] Shi H, Li ZS, Kou JH, Ye JH, Zou ZG (2010) Facile synthesis of single-crystalline  $\text{Ag}_2\text{V}_4\text{O}_{11}$  nanotube material as a novel visible-light-sensitive photocatalyst. *J Phys Chem C* 115(1):145–151
- [44] Xue JJ, Ma SS, Zhou YM, Zhang ZW, He M (2015) Facile photochemical synthesis of Au/Pt/g- $\text{C}_3\text{N}_4$  with plasmon-enhanced photocatalytic activity for antibiotic degradation. *ACS Appl Mater Interfaces* 7:9630–9637
- [45] Wang D, Xu Z, Luo Q et al (2015) Preparation and visible-light photocatalytic performances of g- $\text{C}_3\text{N}_4$  surface hybridized with a small amount of CdS nanoparticles. *J Mater Sci* 51(2):893–902